Structural and chemical analysis of CdSe/ZnSe nanostructures by transmission electron microscopy

N. Peranio, A. Rosenauer, and D. Gerthsen
Laboratorium für Elektronenmikroskopie, Universität Karlsruhe, Kaiserstrasse 12, D-76128 Karlsruhe, Federal Republic of Germany

S. V. Sorokin, I. V. Sedova, and S. V. Ivanov
A. F. Ioffe Physico-Technical Institute, 194021 St. Petersburg, Russia

(Received 11 January 2000)

A transmission electron microscopy (TEM) study of the structure and chemical composition of 0.5 to 3.0 ML (monolayer) CdSe sheets that are buried in a ZnSe matrix is presented. The CdSe layers were grown by migration-enhanced epitaxy at a growth temperature of 280 °C. We find two-dimensional (2D) $Cd_xZn_{1-x}Se$ layers with a total thickness of approximately 3 nm for all samples independent of the nominal CdSe content that contain inclusions (islands) with an enlarged Cd concentration. Plan-view TEM revealed two types of islands: First, small 2D islands with a lateral size of less than 10 nm, and second, large 2D islands with a lateral size between 30 and 130 nm. The combination of two-beam dark-field imaging and the new composition evaluation by lattice fringe analysis (CELFA) procedure allow the precise measurement of the Cd-concentration profiles of the $Cd_xZn_{1-x}Se$ layers. The CELFA evaluation yields a full width at half maximum value of (10 ± 1) ML. The most probable origin of the broadening is a strong interdiffusion of Cd and Zn with an additional contribution of the segregation of the Cd atoms. The diffusion length of the Cd diffusion in ZnSe during the growth of the ZnSe cap layer is $L_D=(3.6\pm0.8)$ ML and the segregation probability is estimated to be $R=(0.6\pm0.2)$. It is shown that neither objective lens aberrations nor specimen tilt are the main sources for the observed enormous broadening of the CdSe interlayers.

I. INTRODUCTION

Low-dimensional semiconductor structures are at present one of the main research topics in solid-state physics. Most applications of semiconductor nanostructures are found in the field of optoelectronic devices like light-emitting diodes and lasers. The development of the quantum-dot (QD) lasers is expected to lead to an increased quantum efficiency and to lower threshold-current densities. In some high lattice-mismatch heterostructures like In(Ga)As/GaAs, the Stranski-Krastanow growth mode leads to the self-organized formation of QD's.[1,2] The formation of CdSe QD's is likewise expected in the CdSe/ZnSe system that possesses a similar lattice-parameter misfit of $f_a=6.8\,\%$. Several transmission electron microscopy (TEM), photoluminescence spectroscopy, and atomic force microscopy studies were already published (see Refs. 3–11). However, until now there is a lack of direct information on the structure, the distribution of the Cd and Zn in ZnSe-capped CdSe layers, and in particular on the mechanisms determining the Cd distribution, which were analyzed in detail in this study.

II. EXPERIMENTAL SETUP

The epitaxial layers were grown pseudomorphically on GaAs(001) substrates at a temperature of 280 °C. The samples contain a 50 nm thick ZnSe buffer and a 10 nm thick ZnSe-cap layer grown by molecular-beam epitaxy (MBE) at a Se/Zn flux ratio of 1.3. The CdSe epilayer was deposited by migration enhanced epitaxy (MEE) (see Refs. 12–15) with nominal thicknesses of 0.5, 1, 2, or 3 ML (monolayers). Note that the unit ML in the following is understood to correspond to 0.283 nm independently of the Cd concentration x in $Cd_xZn_{1-x}Se$. During the MEE mode, the Se and Cd fluxes were supplied separately with a 10 s interruption.

The TEM cross-section samples were conventionally prepared with Ar^+- or Xe^+- ion milling at an energy of 3 keV in a liquid nitrogen-cooled specimen holder. Plan-view samples were prepared by dimple grinding and subsequent back-side chemical etching in a solution of $1\,H_2O_2(30\%):5\,NaOH$. A Philips CM200 FEG/ST transmission electron microscope was used with a spherical aberration constant $C_S=1.2$ mm and a Scherzer resolution of 0.24 nm. The cross-section images were recorded with an on-line CCD camera with 1024×1024 picture elements.

III. EXPERIMENTAL RESULTS

A. Plan-view imaging

Plan-view images yield an overview of the size distribution and density of the islands. Figures 1(a), (b), (c), (e), and (f) show conventional (220) dark-field images of the sample with nominally 0.5, 1, 2, and 3 ML CdSe. The observed strain contrast can be interpreted in terms of islands. It originates from local lattice bending at the boundary between the island and the ZnSe matrix. Two different kinds of islands are prevailing. First, the micrographs reveal large islands with extensions between 30 and 130 nm [details (ii), (iii), (iv), and (v) in Fig. 1]. The estimated densities of the large islands are $5\times10^9\,cm^{-2}$ (0.5 ML), $9\times10^9\,cm^{-2}$ (1 ML), $7\times10^9\,cm^{-2}$ (2 ML), and $2\times10^9\,cm^{-2}$ (3 ML). Second, we found small islands with a size of less than 10 nm. In con-

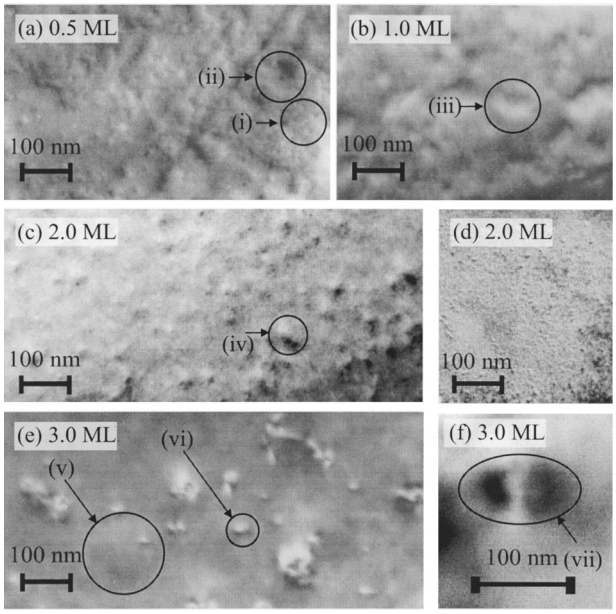

FIG. 1. TEM plan-view images of the samples with nominal $Cd_xZn_{1-x}Se$ layer thicknesses of (a) 0.5 ML, (b) 1 ML, (c) and (d) 2 ML, and (e) and (f) 3 ML. (a), (b), (c), (e), and (f) are (220) dark-field images and (d) is a (220) (**g**/4**g**) weak-beam image.

ventional (220) dark-field images, the small islands show only a faint contrast [e.g., inside region (i) of Fig. 1(a)]. The density of small islands is approximately $7\times10^{10}\,\mathrm{cm}^{-2}$ (0.5 ML) and $4\times10^{11}\,\mathrm{cm}^{-2}$ (2 ML) corresponding to average island distances of 38 nm and 15 nm. The small islands are more clearly visible in $g/4g$ weak-beam (WB) micrographs [see Fig. 1(b)] due to the smaller contrast widths that are obtained by the WB imaging. We also found the contrast features of small islands embedded in large islands. In the 3 ML sample, large islands with a pronounced ''coffee-bean'' strain contrast are in addition observed at a low density of approximately $6\times10^{8}\,\mathrm{cm}^{-2}$ [region (vii) in Fig. 1(f)]. The coffee-bean contrast could be indicative of the three-dimensional (3D) nature of these islands while the other islands can be expected to be of rather flat shape which will be confirmed in Secs. III B and III C 2. The plan-view images did not show any defects in the samples containing 0.5, 1, and 2 ML CdSe as expected for pseudomorphically grown heterostructures. A low defect density of $2\times10^{9}\,\mathrm{cm}^{-2}$ was observed in the 3 ML structure.

B. (002) dark-field images

Conventional dark-field images of cross-sectional specimens were used for a first estimation of the Cd distribution. A two-beam condition with a strongly excited and centered (002) beam was used for the imaging. Starting with a cross-section sample with a [100]-zone axis orientation, the specimen was tilted approximately 5° around the [001] direction. Note that a tilt around the [001] direction does not cause an artificial broadening of the $Cd_xZn_{1-x}Se/ZnSe$ interfaces (projected along the electron-beam direction) in contrast to a tilt around the [010] direction.

Figure 2 shows (002) dark-field images of all investigated samples. The CdSe epilayer can be clearly identified by its lower brightness. The observed contrast in the (002) dark-field micrographs can be attributed to different atomic scattering factors of Cd and Zn. In a kinematic approximation, the structure factor F_{hkl} for the sphalerite structure is given by

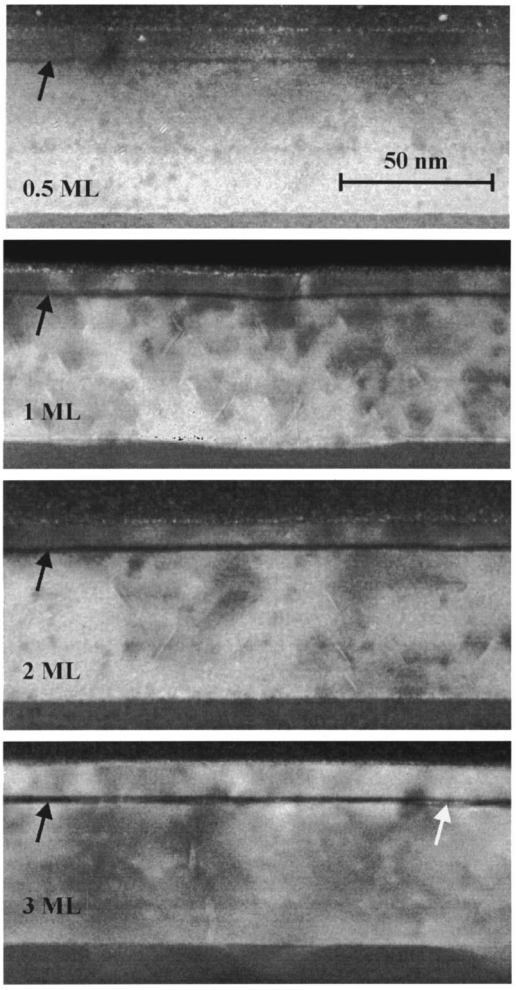

FIG. 2. TEM cross-sectional (002) dark-field images of all investigated samples with the nominal CdSe content indicated on the micrograph. The black arrows indicate the $Cd_xZn_{1-x}Se$ layer. The white arrow marks a region with a Cd concentration larger than 41 %.

$$F_{hkl}=4[f_{Cd_xZn_{1-x}}+f_{Se}\exp\{i2\pi(h+k+l)/4\}], \qquad (1)$$

where $f_{Cd_xZn_{1-x}}$ and f_{Se} are the atomic scattering factors of the two-atomic basis. In the case of the (002) reflection we obtain $F_{002}=4(f_{Cd_xZn_{1-x}}-f_{Se})$. Therefore, the intensity of the (002) reflection strongly depends on the chemical composition and is called a ''chemically sensitive'' reflection. It is appropriate to note that this is not the case for an electron-beam direction close to, e.g., a ⟨110⟩-zone axis where an artificial excitation of the (002) beam can occur due to multiple scattering.

Bloch-wave calculations with the EMS program package[16] revealed that the image intensity I for $Cd_xZn_{1-x}Se$ normalized with respect to the intensity in ZnSe, is given by $I=6(x-0.41)^2$ (x is the Cd concentration) for sample thicknesses below 50 nm as displayed in Fig. 3. A value of $I=1$ represents the ZnSe. The image intensity I reaches its

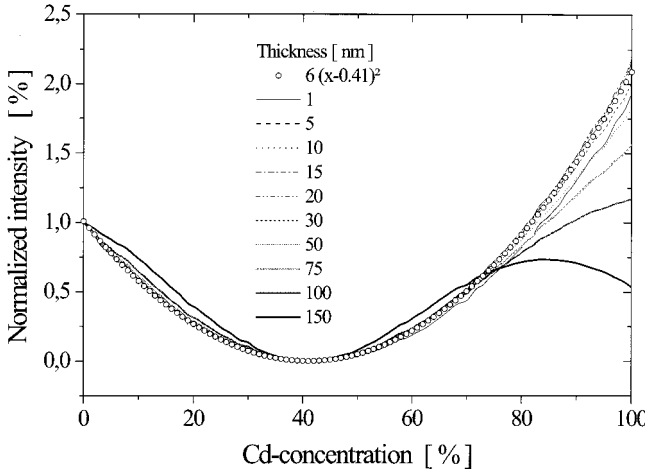

FIG. 3. Normalized intensity of the (002) beam plotted versus the Cd concentration calculated with EMS for different sample thicknesses.

minimum at $x=0.41$. Regions with a Cd concentration $x>0.41$ (e.g., in islands) would appear with a bright contrast within the dark background of the epilayer.

Note that it is difficult to identify individual islands in Fig. 2. Distinct concentration fluctuations along the $Cd_xZn_{1-x}Se$ can only be seen in the microgaph of the 3 ML sample where we find some regions with a Cd concentration larger than 41 % (white arrow in Fig. 2). These observations indicate that most islands observed in plan-view micrographs (see Fig. 1) are due to rather small concentration fluctuations inside a 2D $Cd_xZn_{1-x}Se$ layer with a quite homogeneous thickness. Most probably, only few islands with strongly pronounced strain contrast, like that depicted in Fig. 1(f), are 3D islands.

Figure 4 shows the line scans of the image intensities across the $Cd_xZn_{1-x}Se$ layer in growth direction normalized with respect to the intensity in the ZnSe. The line scans represent intensity profiles that were averaged from different positions along the $Cd_xZn_{1-x}Se$ layer. We find qualitatively a decrease of the minimum intensity (equivalent to an increasing maximum of the Cd-concentration profile) with an increasing (nominal) amount of CdSe. The full widths at half maximum (FWHM) of the intensity profiles of (2.3 ± 0.3) nm are similar for all samples and reveal a significant broadening in comparison to the nominal layer thickness.

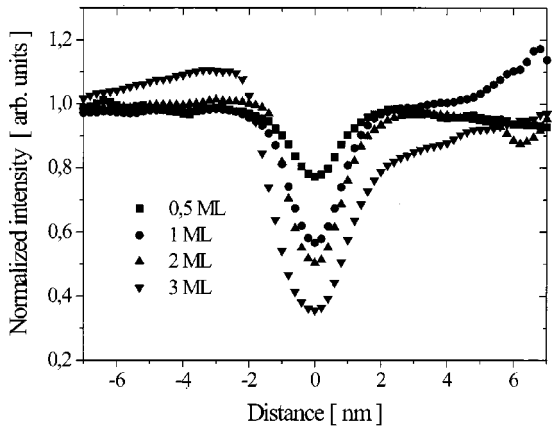

FIG. 4. Intensity linescans of (002) dark-field images across the $Cd_xZn_{1-x}Se$ layer for all samples in growth direction.

Note that Fig. 3 cannot be used for an accurate determination of the Cd concentration from Fig. 4 because of inelastic electron scattering. The objective lens possesses different focal lengths for inelastically and elastically scattered electrons. Therefore, inelastically scattered electrons cause an (incoherent) diffuse background intensity I_{inel} in the image. These additional electrons lead, for example, to a nonvanishing image intensity for a Cd concentration of 41 %. The effect of inelastic scattering on the interpretation of Fig. 4 is readily estimated by assuming that I_{inel} is constant over each line scan and $x<0.41$. Then, the normalized image intensity shown in Fig. 4 is given by

$$I=\frac{I_{\mathrm{el}}+I_{\mathrm{inel}}}{I_0+I_{\mathrm{inel}}}, \tag{2}$$

where I_{el} is the intensity of elastically scattered electrons and I_0 is I_{el} for $x=0$. With I' being the normalized intensity without inelastic scattering displayed in Fig. 3 we find

$$\frac{I}{I'}=\frac{1+I_{\mathrm{inel}}/I_{\mathrm{el}}}{1+I_{\mathrm{inel}}/I_0}. \tag{3}$$

From Eq. 3 we deduce that $I\leqslant I'$ because $I_{\mathrm{el}}\leqslant I_0$. Therefore, the interpretation of Fig. 4 with the $I(x)$ dependency shown in Fig. 3 leads to concentration values that are too small. Nevertheless, (002) dark-field imaging provides an easy-to-apply method to obtain a semiquantitative impression of the Cd concentration in thin $Cd_xZn_{1-x}Se$ layers.

C. Composition evaluation by lattice fringe analysis

The chemical sensitivity of the (002) reflection can be further exploited to quantify the composition at higher resolution and better accuracy by using an electron interference pattern. This approach possesses two advantages compared to the dark-field technique. First, the effect of inelastic scattering is reduced because inelastically scattered electrons approximately can be considered as incoherent. Secondly, the generation of images with a periodic contrast pattern enables an effective noise reduction by the Wiener-filtering technique.[17] In the Fourier-transformed images, the significant information then is localized in the reflections, whereas the noise spreads over the whole area.

1. Explanation of the analysis procedure

The CELFA method is described for $In_xGa_{1-x}As$ in Refs. 18 and 19. A detailed explanation of the CELFA procedure as well as its application to $Cd_xZn_{1-x}Se$ can be found in Ref. 20. Here we only give a brief outline of the principle of this technique.

The CELFA method is based on high-resolution TEM lattice-fringe images resulting from a three-beam condition with the (000), (020), and (040) reflections. A cross-section specimen with a [100]-zone axis orientation is tilted by 3° to 6° around an axis parallel to the [010] direction (see Fig. 5). Subsequently, it is adjusted in such a way that only the incident beam and the (040) reflection are strongly excited. The (020) reflection is centered on the optic axis to minimize the effects of objective lens aberrations. Note that the specimen

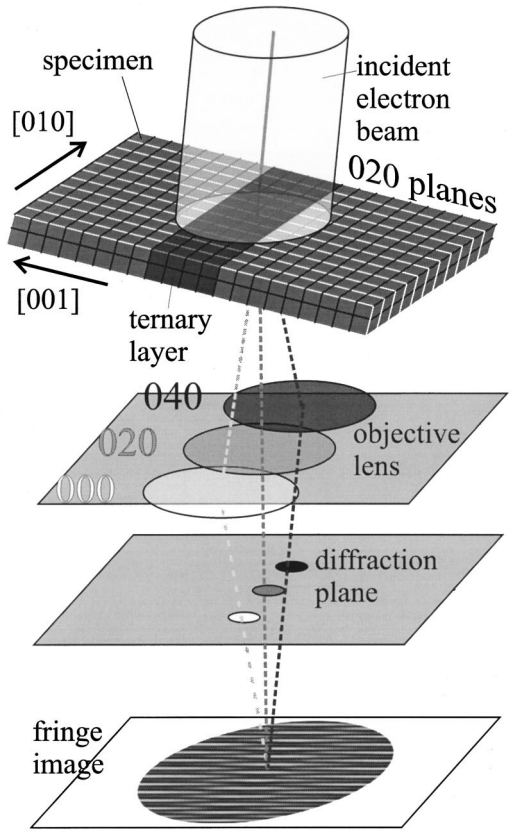

FIG. 5. Sketch showing the imaging condition used for the CELFA method.

tilt here is performed around an axis perpendicular to that used in Sec. III B. A different tilt axis is chosen because the (002)-plane distances depend on the Cd concentration of the $Cd_xZn_{1-x}Se$ layer. However, the effect of different lattice parameters on the image pattern can be neglected if the (020) lattice planes are used for the imaging that have identical distances in the interlayer and the ZnSe matrix in pseudomorphically grown structures. A focus series of 10 images with a defocus stepsize of typically 10 nm is recorded. The amplitude A_{020} of the (020) reflection in the Fourier transform (diffractogram) of the image n of the defocus series is then given by:[20]

$$A_{020}=T_{020}a_{020}\times\sqrt{a_{040}^2+a_{000}^2+2a_{040}a_{000}\cos(\varphi_n)},$$

$$\varphi_n=-2\chi_n+2p_{020}-p_{000}-p_{040},$$

$$\chi_n=\pi\Delta f_n\lambda\mathbf{g}_{020}{}^2+\frac{\pi}{2}C_S\lambda^3\mathbf{g}_{020}{}^4, \tag{4}$$

where the a_{0j0} are the amplitudes and p_{0j0} the phases of the coefficients of the Fourier-transformed exit wave function ($j=0,2,4$). T_{020} is a real factor taking into account incoherency effects, Δf_n the objective lens defocus for the nth image of the defocus series, $\mathbf{g}_{020}$ the reciprocal lattice vector corresponding to the (020) reflection, and λ the De Broglie wavelength of the electrons. χ_n is the phase shift introduced by the spherical aberration of the objective lens and the defocus. Equation (4) shows that the amplitude A_{020} of the (020) reflection in the diffractogram is proportional to the amplitude a_{020} of the chemically sensitive (020) beam.

The evaluation of the local Cd concentration is performed in the following way:

1. All images of the series are subdivided into image cells of 0.283 nm×0.283 nm (≙1 ML×1 ML in GaAs) size. Each cell is transformed into a quadratic cell with a typical size of 16^2 pixels using the algorithm described in Ref. 21. The cells are Fourier transformed and the amplitude of the (020) reflection of each cell diffractogram yields a local value for A_{020}.

2. An approximate specimen thickness and the values χ_n are determined from the defocus-dependent oscillation of A_{020} (see Refs. 19 and 20).

3. The amplitudes a_{0j0} and phases p_{0j0} are calculated for the estimated specimen thickness and Cd concentrations between 0 and 100 % with a stepsize of 1 % using the Bloch-wave method of the EMS program package.[16]

4. One image N of the defocus series that corresponds to a maximum of the A_{020} oscillation is used for the further evaluation. In order to compensate for spatial variations of the specimen thickness and defocus, T_{020} is regarded as fit parameter and a local map of T_{020} is calculated from Eq. (4) inside the ZnSe buffer and cap layers (see Refs. 19 and 20) where the Cd concentration $x=0$ is known. An overall map of T_{020} is obtained by interpolation inside the $Cd_xZn_{1-x}Se$ region.

5. Finally, Eq. (4) is used to obtain the local Cd concentration x for each image cell.

It was shown in Ref. 19 that an error of the estimated specimen thickness t as well as local thickness variations only weakly affect the measured composition if the thickness dependence of $a_{020}(x,t)/a_{020}(0,t)$ is small. Figure 6(a) shows that this prerequisite is well fulfilled for $Cd_xZn_{1-x}Se$. Figure 6(b) displays a color-coded map of the estimated relative maximum error $\Delta x/x$ of the composition determination per nm error Δt of the thickness measurement whose calculation is explained in Ref. 19. For example, measured values $x=20\%$ and $t=(15\pm10)$ nm yield an error $\Delta x=0.0016[\mathrm{nm}^{-1}]\ 10\,\mathrm{nm}\,20\%=0.3\%$, i.e., $x=(20\pm0.3)\%$. Therefore, the error of the thickness determination is negligible for the measurements presented in the following.

2. Experimental results

Figure 7 depicts color-coded maps of the Cd distribution for all investigated samples. Note that the color coding is not identical for all images. In particular for the 0.5 and 1 ML samples the green color denotes a Cd concentration of only 2 to 4 %. In general, we find an approximately 3 nm thick $Cd_xZn_{1-x}Se$ layer (2D-L) that contains inclusions with larger Cd concentration (islands). In the 2 ML sample we find pronounced small islands with a lateral size of ≈8 nm [see Fig. 7(d)]. Figure 7(c) gives an example for a large-scale fluctuation with less pronounced small inclusions in the same specimen. The white-dotted lines in Figs. 7(b) and 7(e) indicate that some of the inclusions probably are found in the vicinity of interface steps. Figure 7 also visualizes the 2D

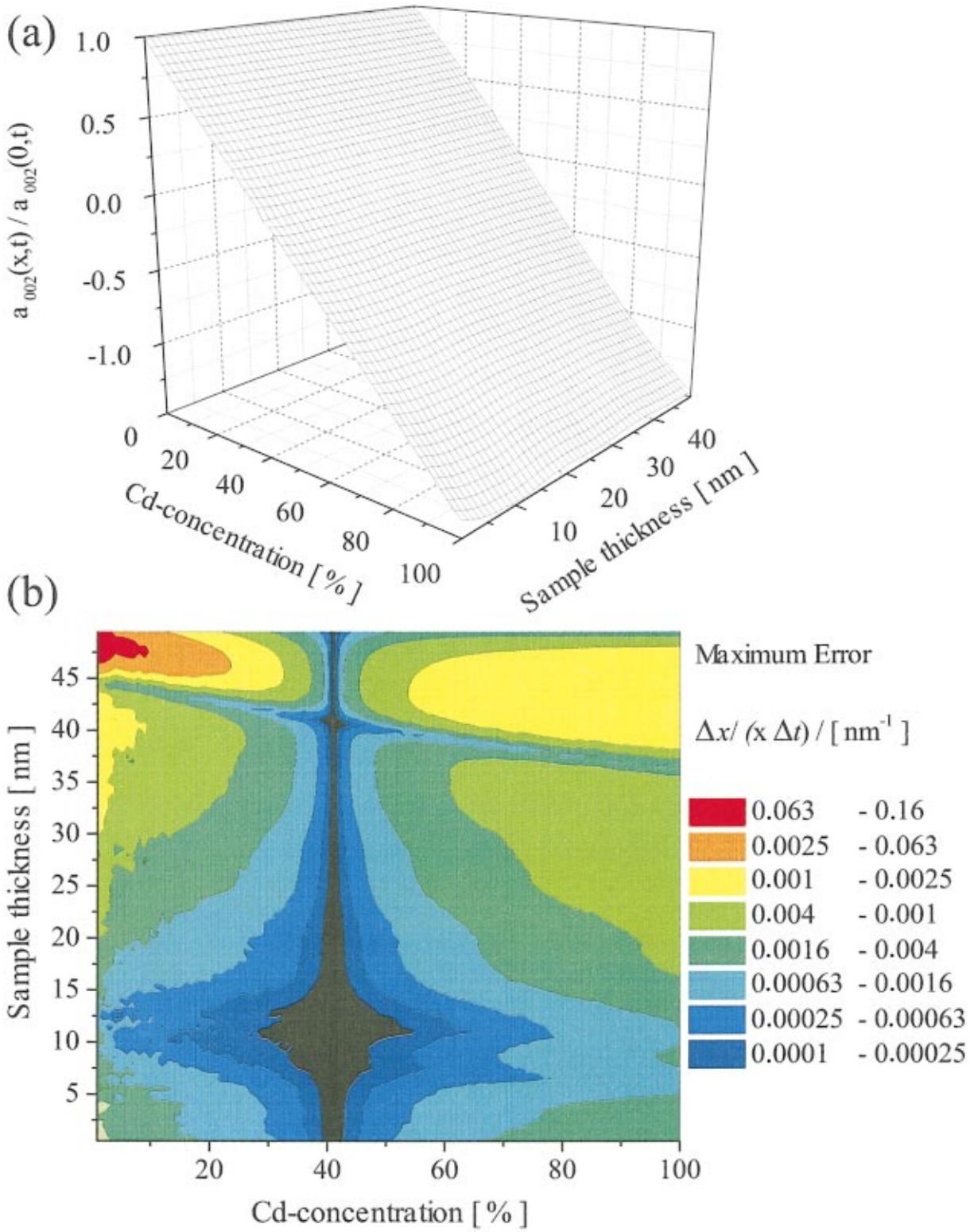

FIG. 6. (Color) (a) Values for $a_{020}(x,t)/a_{020}(0,t)$ plotted versus the Cd concentration x and the specimen thickness t. (b) Color-coded diagram showing the maximum error Δx of the measured Cd concentration x due to uncertainties Δt of the thickness measurement, plotted versus the sample thickness t and the Cd concentration x.

character of the islands whose height does, in general, not exceed the thickness of the $Cd_xZn_{1-x}Se$ layer.

Figure 8 contains typical Cd-concentration profiles of the 2D-L's for each of the four samples which were determined in regions between the islands. The total Cd content is computed by the integration of the profiles. Table I summarizes the results obtained for the 2D-L's and islands. Table I reveals that the maxima of the Cd-concentration profiles x_{max} increase with the nominal CdSe content. However, they always remain below 20%. Generally, the total amount of CdSe in the QW is 70–80 % of the nominal value. The total Cd content in the center of the islands significantly exceeds

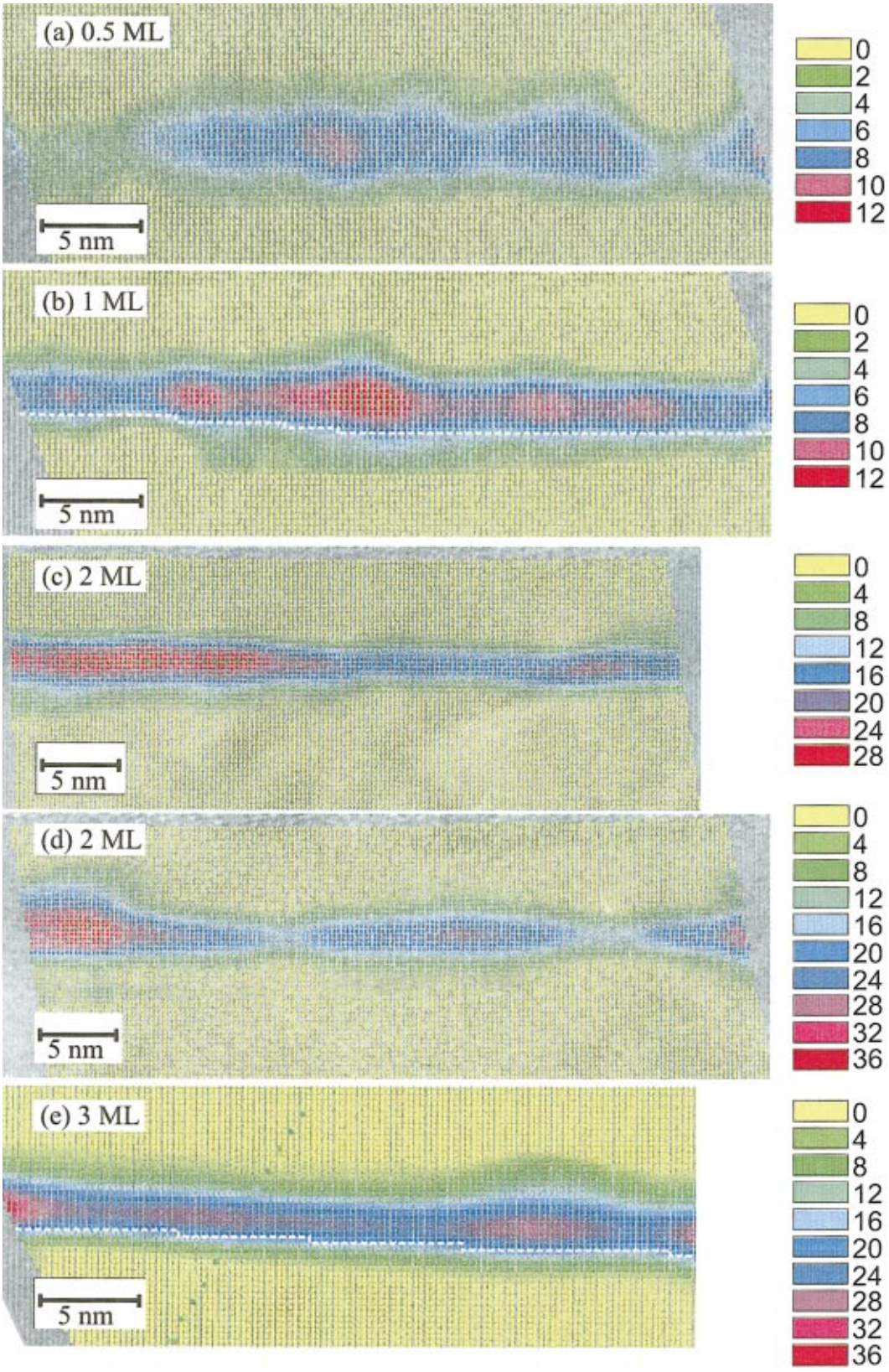

FIG. 7. (Color) Color-coded maps of the local Cd concentration for all investigated samples. Each colored square corresponds to an area of 0.283 nm×0.283 nm (≙1 ML×1 ML in GaAs). (c) and (d) reveal large-scale and short-scale fluctuations of the Cd concentration in the 2 ML sample, respectively.

the nominal amount. Therefore, 20–30 % of the Cd must beconcentrated in the islands, besides possibly the 0.5 ML sample. All profiles of the 2D-L's have a FWHM of ≈10 ML and exhibit a weakly pronounced asymmetry because the transition from the ZnSe buffer to the $Cd_xZn_{1-x}Se$ layer is steeper than that towards the cap layer. It is appropriate to

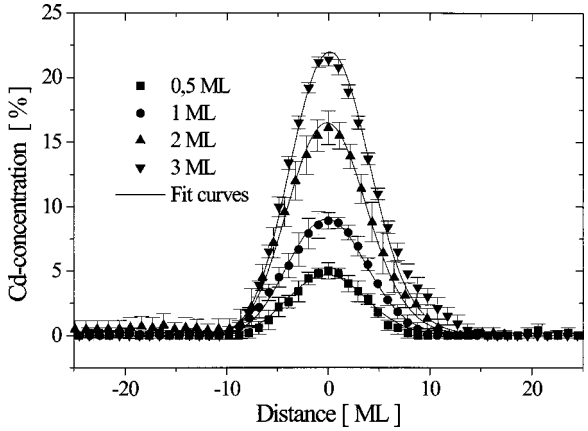

FIG. 8. Cd-concentration profiles of the 2D-L's with fitted profiles taking into account a diffusion length $L_D = 3.6$ ML, a segregation probability $R = 0.6$, and the sample tilt of 6° at a specimen thickness of 20 nm (see Sec. IV A).

note that the measured concentrations are averaged along the electron-beam direction, which means that the actual concentrations inside the islands may be higher.

IV. DISCUSSION

A. Interpretation of the concentration profiles

The most striking result of the Cd-concentration profiles (see Fig. 8 and Table I) is a significant broadening of the CdSe layer that is most likely induced by interdiffusion. The general solution of Fick's laws for a given concentration profile $\varphi(r)$ at the time $t=0$ is given by

$$x_{\mathrm{diff}}(i,L_D)=\frac{1}{\sqrt{\pi}L_D}\int_{-\infty}^{\infty}\varphi(r)\exp\left\{-\frac{(r-i)^2}{L_D^2}\right\}dr, \quad (5)$$

where i and r are distances in growth direction in [ML]. $L_D[\mathrm{ML}]=2\sqrt{Dt}$ is the diffusion length with D being the (composition-independent) diffusion coefficient and t the duration of the diffusion process. Using the initial Cd-concentration profile of an ideal epilayer of N monolayers CdSe, Eq. (5) constitutes a fit curve for the experimental profiles with L_D as fit parameter:

$$x_{\mathrm{diff}}^{\mathrm{idea}}(i,L_D)=\frac{1}{2}\left\{\mathrm{erf}\left(\frac{i+\frac{N}{2}}{L_D}\right)-\mathrm{erf}\left(\frac{i-\frac{N}{2}}{L_D}\right)\right\}. \quad (6)$$

TABLE II. Fit values of the diffusion length L_D and the segregation probability R. With the exception of the second column, a sample tilt of 6° was taken into account at a maximum sample thickness of 20 nm.

	Diffusion L_D[ML]		Segregation and diffusion	
Sample	Without tilt	With tilt	L_D[ML] with tilt	R with tilt
0.5 ML	5.5±0.4	4.5±0.6	3.4±0.7	0.6±0.1
1 ML	5.1±0.5	3.9±0.7	3.5±0.9	0.5±0.1
2 ML	5.6±0.6	4.6±0.7	4.0±0.8	0.5±0.1
3 ML	5.6±0.6	4.5±0.8	3.6±0.9	0.6±0.2

The evaluated diffusion lengths are given in the second column of Table II. Taking into account the error bars, the results are identical for all four samples yielding an average $L_D \approx 5.5$ ML. This result is in contrast to diffusion coefficients measured in earlier studies (see Refs. 22–25) that lead to diffusion lengths of about 0.08 ML assuming a temperature of $T=280\,°C$ and a duration of the diffusion of $t=3$ min. Possible origins for this discrepancy will be discussed in Sec. IV C.

The influence of the sample tilt around an axis parallel to [010] has to be considered with respect to a possible artificial broadening of the measured profile. However, the (002) dark-field images in Fig. 2, that were obtained by tilting around the perpendicular [001] direction, also reveal a strong broadening (see Fig. 4) indicating that the tilt is not the main source of the broadening.

For the calculation of the effect of tilt on the measured concentration profile of a homogeneous 2D-$Cd_xZn_{1-x}Se$ layer we assume that the $Cd_xZn_{1-x}Se$/ZnSe interface is parallel to the (001) plane. The tilt of a specimen with a thickness t and an initial [100]-zone axis orientation by an angle β around the [010] direction (see Fig. 5) yields a profile

$$x_{\mathrm{tilt}}(i)=\frac{1}{t}\int_0^t x_{\mathrm{notilt}}\left(\frac{i}{\cos\beta}+\tau\tan\beta\right)d\tau \approx \frac{1}{\Delta r}\int_i^{i+\Delta r} x_{\mathrm{notilt}}(r)\,dr, \quad (7)$$

where $\Delta r = t\tan\beta$ and $x_{\mathrm{notilt}}(r)$ is the projected concentration profile of the untilted specimen. Using $x_{\mathrm{notilt}}=x_{\mathrm{diff}}^{\mathrm{ideal}}$ Eq. (7) yields

TABLE I. Maximum concentrations $x_{\max}$ and sizes of the 2D-L's and islands. The amount of Cd is obtained by the integration of Cd-concentration profiles and is given in equivalents of [ML CdSe].

	2D layer			Islands		
Sample	$x_{\max}$ [%]	Cd amount [ML CdSe]	FWHM [ML]	$x_{\max}$ [%]	Cd amount [ML CdSe]	Diameter [nm]
0.5 ML	4±2	0.5±0.2	9±2	8±3	1.0±0.4	7±5
1 ML	7±2	0.7±0.1	10±1	10±1	1.0±0.1	6±2
2 ML	16±2	1.6±0.3	10±1	25±4	3.1±0.9	12±4
3 ML	19±4	2.0±0.4	10±1	35±7	4.8±1.4	9±2

$$x_{\mathrm{diff,tilt}}^{\mathrm{ideal}}=\frac{L_D}{2\Delta r}\left\{f\left(\frac{i+N/2+\Delta r}{L_D}\right)-f\left(\frac{i+N/2}{L_D}\right)-f\left(\frac{i-N/2+\Delta r}{L_D}\right)+f\left(\frac{i-N/2}{L_D}\right)\right\},$$

$$f(x)=x\,\mathrm{erf}(x)+\frac{1}{\sqrt{\pi}}(e^{-x^2}-1). \tag{8}$$

Taking into account a maximum tilt angle of $\beta=6°$ and a maximum sample thickness of $t=20\,\mathrm{nm}$, and again using L_D as fit parameter, we obtained the diffusion lengths listed in the third column of Table II yielding a mean value of $L_D \approx 4.4\,\mathrm{ML}$.

The asymmetry of the measured concentration profiles indicates that segregation has to be considered as a third effect to contribute to the broadening of the CdSe sheets. The conventional surface segregation (see e.g., Ref. 27) due to the replacement of Cd atoms from the underlying monolayer by newly deposited Zn atoms, appears to be unlikely under the Se-rich ZnSe growth conditions used. However, Cd segregation may occur during the ZnSe overgrowth on the CdSe-terminated surface containing islands due to the strain-induced Cd extrusion by neighboring-in-plane Zn atoms at the strongly lattice-mismatched CdSe/ZnSe lateral boundaries. Following the general formalism of Muraki *et al.*,[26] the Cd-concentration profile can be described by

$$x^{\mathrm{segr}}(i)=\begin{cases}0 & : \ i<0\\ x_0(1-R^i) & : \ 0<i\leqslant N,\\ x_0(1-R^N)R^{i-N} & : \ i>N,\end{cases} \tag{9}$$

where R is the segregation probability and N the number of deposited monolayers of $\mathrm{Cd}_{x_0}\mathrm{Zr}_{1-x_0}\mathrm{Se}$. However, it was not possible to fit the measured profiles solely on the basis of Eq. (9) with sufficient accuracy. Therefore, we suppose that both diffusion and segregation are involved. To check this assumption we made the approximation that the initial Cd distribution $\varphi(r)$ is formed by segregation [Eq. (9)] and subsequently is broadened by interdiffusion according to Eq. (5). The resulting profile $x_{\mathrm{diff}}^{\mathrm{segr}}$ was inserted in Eq. (7) using $x_{\mathrm{notilt}}=x_{\mathrm{diff}}^{\mathrm{segr}}$ in order to take into account the effect of the specimen tilt. Both, the segregation probability R and the diffusion length L_D, are treated as fit parameters. Again, we assumed a tilt angle of 6° and a sample thickness of 20 nm. This model yields the best agreement between the fit curve and the experimental data leading to mean values of $L_D = 3.6\,\mathrm{ML}$ and $R=0.6$ (see Table II, columns 4 and 5).

B. Errors due to the electron-microscopic imaging

1. The effect of objective lens aberrations

The aberration of the objective lens as well as Fresnel fringes constitute other sources of error that could lead to a broadening of the observed profiles. Incoherency effects yield a damping of the transfer function at high spacial frequencies mainly causing a broadening of chemically abrupt transition regions. Fresnel fringes are induced by steps of the mean inner potential either at the interface between specimen and vacuum or at internal interfaces between different materials. They occur for defoci $|\Delta f|>0$. Their intensity and spacing depends on the inner potential step height as well as on the shape of the chemical transition at the interface. It should be noted that these effects apply to both the (002) dark-field imaging and to the CELFA technique. Profiles of A_{002} are compared in Fig. 9 for a simulated defocus series for an ideal, 2 ML thick CdSe layer buried in ZnSe (upper curves) with measured profiles of the 2 ML sample (lower curves). Obviously, the simulated profiles deviate from the initial profile. However, these deviations do not explain the width of the experimental profiles. Simulations have shown that the deviation of the simulated profiles from the initial profiles decrease for less abrupt transition regions.

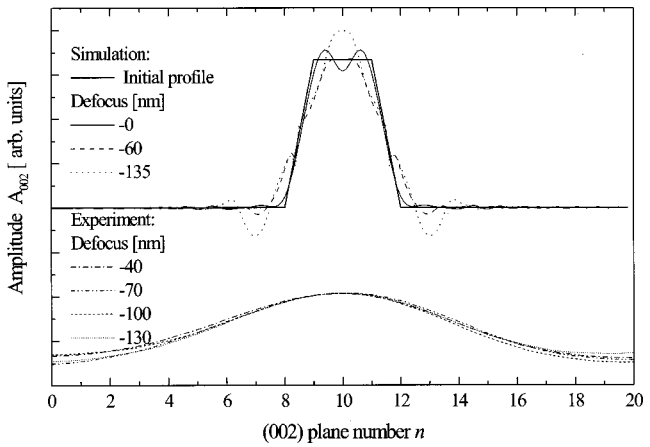

FIG. 9. Upper curves: Profiles of the amplitude A_{020} simulated for a 2 ML thick CdSe interlayer buried in ZnSe for different values of the objective lens defocus Δf. A linear concentration profile was assumed inside the transition regions between ZnSe and CdSe. The shape of the initial profile is indicated by the bold solid curve. The specimen thickness was assumed to be 10 nm. The microscope parameters were: Accelerating voltage $U_b=200\,\mathrm{kV}$, $C_S=1.2\,\mathrm{mm}$, semiconvergence angle of the electron beam 3 mrad and defocus spread 7 nm. The electron-microscopic imaging was simulated with the EMS program package. Lower curves: Experimental profiles of a defocus series of the 2 ML sample.

2. Specimen tilt and nonstatistical distribution of Cd *atoms*

We explained in Sec. III C 1 that Bloch-wave simulations are used to calculate the amplitudes a_{0j0} of the beams that contribute to the image. These values are used to determine the Cd concentration x from the experimental image using Eq. (4). The Bloch-wave calculations imply a statistical distribution of the Cd and Zn atoms along the electron-beam direction. This assumption is not fulfilled for an interface that is tilted against the electron beam as illustrated in Fig. 10. Figure 10 shows as an example a 7 nm thick $\mathrm{Cd}_{0.3}\mathrm{Zn}_{0.7}\mathrm{Se}$ layer that is tilted against the electron-beam direction. Obviously, the distribution of Cd and Zn atoms is not statistical in the regions of the tilted interface. For the upper interface, all Cd atoms are concentrated in the upper part of the TEM sample in contrast to the lower interface where the Cd atoms are located in the lower part of the sample.

To estimate the effect of the nonstatistical distribution, an atomic model was generated according to Fig. 10 assuming a

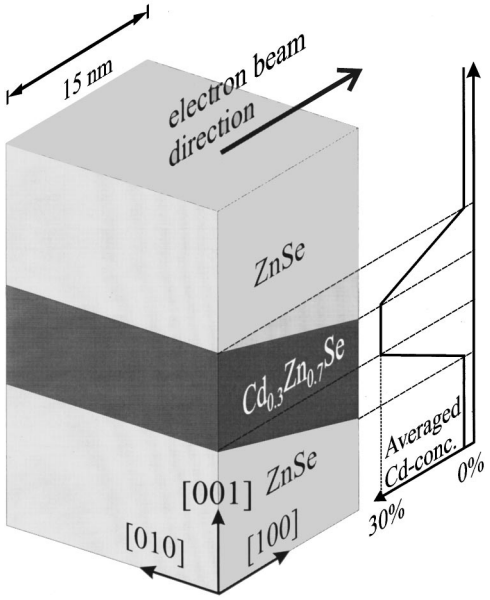

FIG. 10. Model of a 15 nm thick TEM specimen containing a 7 nm $Cd_{0.3}Zn_{0.7}Se$ layer buried in ZnSe that is tilted towards the electron beam direction. The displayed configuration was used to derive an atomic model to estimate the effect of a nonstatistical distribution of Cd and Zn atoms along the electron-beam direction by multislice iterations. Furthermore, the figure contains a sketch of the projected Cd concentration obtained by averaging along the electron beam direction.

tilt of 5°. On the basis of this model, simulations with the multislice algorithm of the EMS program package[16] were then carried out assuming a strongly excited (004) and transmitted beam. From the resulting exit wave function, a profile (along the [001] direction) of the amplitude a_{002} of the (002) beam, normalized with respect to the local value of $\sqrt{a_{000}^2+a_{002}^2+a_{004}^2}$, was extracted. Similar to the CELFA evaluation of an experimental image, a table of analogously normalized values of the (002) reflection was calculated by Bloch-wave simulations (now assuming a statistical distribution of Cd atoms) for Cd concentrations between 0 and 100 % and with a stepsize of 1 %, for a sample thickness of 15 nm and the imaging conditions as given above. In analogy to the CELFA technique, the profile of normalized a_{002} values (obtained with the multislice algorithm) was evaluated with the table (obtained by the Bloch-wave method). Figure 11 displays the resulting Cd-concentration profile as well as the ''true'' concentration profile that is also sketched in Fig. 10. Obviously, the evaluated profile agrees well with the initial ''true'' profile. Note that the deviation that is visible for the largest concentrations is 1 %, which is equal to the stepsize of the calculated table. This error is most likely due to a small deviation between the multislice approximation and the (more precise) Bloch-wave calculation. These results clearly demonstrate that the effect of a nonstatistical distribution of Cd atoms is small for a Cd concentration of 30 %.

The effect of a nonstatistical distribution of atoms was investigated analytically in a projected-potential approximation by Coene *et al.*[28] They found that it is a second-order contribution to the wave function that is proportional to

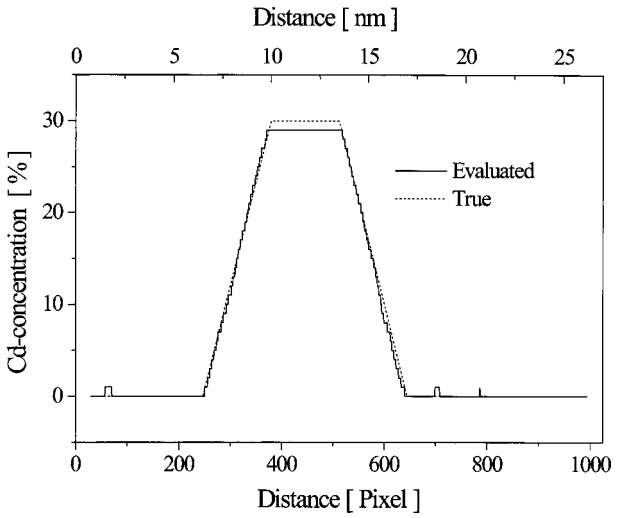

FIG. 11. Cd-concentration profile obtained from the evaluation of a simulated exit wave function. The wave function was simulated by the multislice algorithm on the basis of an atomic model generated according to Fig. 10. The good agreement between evaluated and true profiles indicates the weak influence of the nonstatistical distribution of Cd atoms.

$$\theta_2=\Delta\int_0^z dz'\int_0^{z'}\{V(\mathbf{R},z'')-\langle V(\mathbf{R})\rangle\}dz'',$$

$$\langle V(\mathbf{R})\rangle=\frac{1}{z}\int_0^z V(\mathbf{R},z')dz', \tag{10}$$

where $V(\mathbf{R},z'')$ is the crystal potential, $\mathbf{R}$ the coordinate in the foil plane, Δ the Laplacian operating in the plane of the foil, and z the coordinate in electron-beam direction. From Eq. (10) we estimate that the effect is even smaller for Cd concentrations below 30 %.

C. Comparison with previous results

A similar broadening of CdSe layers was already observed *in situ* in MBE-grown CdSe layers by reflection high-energy electron diffraction (Ref. 22) where an amount of Cd equivalent to 1.4 ML CdSe was found to be distributed over a 6 ML thick transition region towards the ZnSe-cap layer. Kuttler *et al.*[25] showed that the diffusion of Cd in ZnSe is governed by group-II vacancies and depends strongly on the epilayer doping and the atmosphere prevailing during the annealing process. An acceleration of the Cd diffusion by about four orders of magnitude in *N*-doped samples was attributed to a Fermi-level effect, which changes the charge state of the vacancies due to the *p*-type doping.

The diffusion length observed in our paper corresponds to the highest values found in *N*-doped layers, although the samples in our study are undoped. There are two possible explanations for the large diffusion lengths. The first and probably the main effect could be related to the nonequilibrium conditions during the MEE and MBE growth, which could produce an anomalously high density of group-II vacancies within the CdSe layer leading to a strong acceleration of the interdiffusion. The ''annealing'' duration of only 3 min at a very low temperature of 280 °C to grow the ZnSe

cap layer (in contrast to the high annealing temperatures and 2 h annealing duration in the experiments by Kuttler *et al.*,[25]) cannot be expected to yield diffusion distances that are representative for thermal equilibrium conditions. The second reason could be related to the large band bending close to the growth surface, which could induce a charge state of the vacancies comparable to that in *p*-type layers (surface-induced Fermi-level effect).

V. SUMMARY

In summary, we observed that MEE-grown CdSe epilayers with a nominal thickness between 0.5 and 3 ML embedded in ZnSe consist of a 2D layer broadened up to a FWHM of $\approx$10 ML. The $Cd_xZn_{1-x}Se$ layers contain inclusions with an enlarged Cd concentration and with a size of $\leqslant$10 nm and large 2D islands with a lateral extension between 30 and 130 nm. The density of the small islands is in the order of $10^{11}\,cm^{-2}$. The density of large-scale inclusions varies between $2\times10^{9}\,cm^{-2}$ and $9\times10^{9}\,cm^{-2}$, depending on the nominal CdSe content.

The chemical analysis with the CELFA method revealed that the maximum Cd concentration in the $Cd_xZn_{1-x}Se$ layers increases from 4% to 19% with the nominal CdSe content and that approximately 20–30 % of the CdSe is contained in islands. The segregation of the Cd with a probability of (60 ± 20)% was detected. However, the dominant process for the layer broadening is a Cd/Zn interdiffusion with a diffusion length of (3.6 ± 0.8) ML at 280 °C. The interdiffusion is possibly accelerated by a high (nonequilibrium) density of group-II vacancies in the CdSe layer and the surface-induced Fermi-level effect.

ACKNOWLEDGMENTS

This work was supported by the Deutsche Forschungsgemeinschaft under Contract No. Ge 841/7. The research in St. Petersburg is supported by RFBR, Program of the Ministry of Science of RF ''Physics of Solid-State Nanostructures'' and by the Volkswagen-Stiftung.

[1] S. Guha, A. Madhukar, and K. C. Rajkumar, Appl. Phys. Lett. **57**, 2110 (1990).
[2] M. Grundmann, O. Stier, and D. Bimberg, Phys. Rev. B **52**, 11 969 (1995), and references therein.
[3] M. Strassburg *et al.*, Appl. Phys. Lett. **72**, 942 (1998).
[4] T. Kümmell *et al.*, Appl. Phys. Lett. **73**, 3105 (1998).
[5] H. Kirmse *et al.*, Appl. Phys. Lett. **72**, 1329 (1998).
[6] S. V. Ivanov *et al.*, J. Appl. Phys. **83**, 3168 (1998).
[7] S. V. Ivanov *et al.*, Appl. Phys. Lett. **74**, 498 (1999).
[8] M. Rabe, M. Lowisch, and F. Henneberger, J. Cryst. Growth **184/185**, 248 (1998).
[9] F. Gindele *et al.*, J. Cryst. Growth **184/185**, 306 (1998).
[10] K. Leonardi *et al.*, Appl. Phys. Lett. **71**, 1510 (1997).
[11] I. Suemune *et al.*, Phys. Status Solidi B **202**, 845 (1997).
[12] J. G. Cody *et al.*, J. Vac. Sci. Technol. B **12**, 1075 (1994).
[13] S. W. Short *et al.*, J. Vac. Sci. Technol. B **12(2)**, 1143 (1994).
[14] S. V. Ivanov *et al.*, J. Appl. Phys. **83**, 3168 (1998).
[15] S. V. Sorokin *et al.*, J. Cryst. Growth **200/201**, 461 (1999).
[16] P. A. Stadelmann, Ultramicroscopy **51**, 131 (1987).
[17] A. Rosenauer *et al.*, Optik **102**, 63 (1996).
[18] A. Rosenauer, U. Fischer, D. Gerthsen, and A. Förster, Ultramicroscopy **72**, 121 (1998).
[19] A. Rosenauer and D. Gerthsen, Ultramicroscopy **76**, 49 (1999).
[20] A. Rosenauer and D. Gerthsen, Adv. Imaging Electron Phys. **107**, 121 (1999).
[21] A. Rosenauer *et al.*, Optik **105**, 99 (1997).
[22] A. Rosenauer *et al.*, J. Cryst. Growth **152**, 42 (1995).
[23] W. E. Martin, J. Appl. Phys. **44**, 5639 (1973).
[24] M. K. Chai *et al.*, Appl. Phys. Lett. **69**, 1579 (1996).
[25] M. Kuttler *et al.*, Appl. Phys. Lett. **71**, 243 (1997).
[26] K. Muraki, S. Fukatsu, Y. Shirakia, and R. Ito, Appl. Phys. Lett. **61**, 557 (1992).
[27] S. V. Ivanov, P. S. Kop'ev, and N. N. Ledentsov, J. Cryst. Growth **111**, 151 (1991).
[28] W. Coene, D. Van Dyck, J. Van Landuyt, and S. Amelinckx, Philos. Mag. B **56**, 415 (1987).